# Long-Lived Quantum Memory Enabling Atom-Photon Entanglement over 101 km of Telecom Fiber

Yiru Zhou,[1,2,*] Pooja Malik,[1,2] Florian Fertig,[1,2] Matthias Bock,[3] Tobias Bauer,[3] Tim van Leent,[1,2]
Wei Zhang,[1,2,4,†] Christoph Becher,[3] and Harald Weinfurter[1,2,5,6,‡]

[1]*Fakultät für Physik, Ludwig-Maximilians-Universität München, Schellingstrasse 4, München 80799, Germany*

[2]*Munich Center for Quantum Science and Technology (MCQST), Schellingstrasse 4, München 80799, Germany*

[3]*Fachrichtung Physik, Universität des Saarlandes, Campus E2.6, Saarbrücken 66123, Germany*

[4]*Hefei National Laboratory, Hefei 230088, China*

[5]*Max-Planck Institut für Quantenoptik, Hans-Kopfermann-Strasse 1, Garching 85748, Germany*

[6]*Faculty of Mathematics, Physics, and Informatics, University of Gdańsk, 80-308 Gdańsk, Poland*

Long-distance entanglement distribution is the key task for quantum networks, enabling applications such as secure communication and distributed quantum computing. In this work, we take a crucial step toward this task by sharing entanglement over long optical fibers between a single $^{87}$Rb atom and a single photon. High fidelity of the atomic state could be maintained during long flight times through such fibers by prolonging the coherence time of the single atom to 10 ms based on encoding in long-lived states. In addition, the attenuation in the fibers is minimized by converting the wavelength of the photon to the telecom S band via polarization-preserving quantum frequency conversion. These improvements enable us to observe entanglement between the atomic quantum memory and the emitted photons transmitted through standard spooled telecom fibers with a length of 101 km with a fidelity of $70.8 \pm 2.4\%$. This fidelity is comparable to recent demonstrations over 20 km, despite the channel loss now significantly exceeding 20 dB. In fact, now the reduction in fidelity is due to detector dark counts rather than loss of coherence of the atom or photon, proving the suitability of our platform to realize city-to-city-scale quantum network links.

## I. INTRODUCTION

Future quantum networks will build on sharing entanglement between distant locations [1], in order to enable tasks such as distributed quantum computing [2,3], quantum cryptography [4–6], and quantum sensing [7,8]. The entanglement is distributed best via photonic channels using free-space satellite connections [9] or optical-fiber links [10]. However, attenuation losses limit point-to-point channel lengths. In the future, quantum repeater schemes using quantum memories and quantum gates at intermediate nodes will enable us to overcome the exponential decay in the distribution rate [11,12]. To date, experimental

realizations of the first components of prospective quantum networks have been demonstrated in various systems, such as atoms, ions, or solid-state systems. This progress began with the development of light-matter interfaces for entanglement generation [13,14], followed by the utilization of photons at telecom wavelengths to distribute light-matter entanglement over tens of kilometers of optical fiber [15–18]. Subsequent achievements have included the generation of high-fidelity entanglement [19–22] and long-distance entanglement [23–26] between two distant memories, the construction of the first three-node network [27,28], and the implementation of a first functional quantum repeater node [29–31].

In this context, neutral atoms have emerged as a highly promising platform to realize a quantum repeater network [32] by demonstrating key ingredients such as efficient light-matter interfaces [33], long memory-storage times [34], arrays of individually addressable atoms [35,36], and high-fidelity gates [37,38].

Today, fiber-based communication is a reliable way to connect distant locations using telecom wavelengths at which the transmission losses are minimal. If one wants

---

to achieve longer distances between users of a quantum network, one needs to devise similar strategies to minimize transmission losses. Therefore, quantum memories and processors at the nodes [32], should either operate at telecom wavelengths [39] or provide quantum frequency conversion (QFC) to telecom wavelengths [40,41]. Since losses in the quantum channel are inevitable, the system has to provide a classical signal-heralding storage or successful entanglement distribution to achieve sufficient efficiency in further processing.

Furthermore, the size of the quantum network dictates the communication times for quantum and heralding (classical) communication signals, necessitating long coherence times for large-scale networks. For example, assuming a speed of light in an optical fiber of $\frac{2}{3}c$, bridging a fiber length on the order of 100 km takes around 1 ms for the two signals. To achieve high fidelity, it requires coherence times much longer than this. Recent experiments have achieved distribution of entanglement over 20 km for atom-photon entanglement [17] and later over 33 km for atom-atom entanglement [24]. In both cases, the distance was limited by the rapidly decreasing atomic coherence and the resulting reduction of entanglement fidelity. Moving forward, it is imperative to improve the coherence time of the atomic quantum state.

In this paper, we present a neutral atom-based quantum network node capable of long-distance entanglement distribution. Entanglement is observed between the quantum states of a single atom and a photon traveling over telecom fiber spools with lengths of up to 101 km. To achieve this, we introduce a long-lived qubit encoding to increase the coherence time for the atomic quantum memory [42] and a highly efficient, state-preserving QFC to telecom wavelengths. This allows us to explore achievable entanglement distribution distances in quantum networks.

## II. QUANTUM NETWORK NODE

### A. Atom-photon entanglement

Our quantum network node consists of a single $^{87}$Rb atom trapped in a tightly focused optical dipole trap (ODT), loaded from a cloud of $^{87}$Rb atoms in a magneto-optical trap (MOT) [Fig. 1(a)]. Once an atom is loaded in the ODT, we begin with the generation of entanglement between the atom and a photon and finish with the analysis of the resulting entangled state [Fig. 1(b)]. This process can be divided into three stages: (i) cooling, (ii) entanglement generation, and (iii) state readout.

During the first step, the atom is further cooled by polarization gradient cooling near zero magnetic fields for a duration of 1 ms. Thereafter, the intensity of the cooling beams is switched off within 1.5 ms, while the trap depth is adiabatically lowered from 2.3 to 0.19 mK, achieving atomic temperatures of around 8 μK. Further, a magnetic

bias field of 244.5 mG is set along the quantization axis, requiring roughly 4 ms for stabilization.

In the next step, entanglement generation [Fig. 1(c)], the atom is first prepared in the ground state $5^2S_{1/2}$ $|F = 1, m_F = 0\rangle$ by optical pumping (approximately 80 % efficiency within 3 μs). Next, it is excited to the state $5^2P_{3/2} |F' = 0, m_{F'} = 0\rangle$ by a short laser pulse [Gaussian pulse, 21 ns full width at half maximum (FWHM)] with an efficiency of 90 %, reducing off-resonant excitation [43]. Subsequently, the atom spontaneously decays to the $F = 1$ manifold via different decay channels, emitting a 780 nm photon, which is collected by a high-NA objective (NA = 0.5) and coupled into a single-mode fiber. Overall, we obtain a collection-and-coupling efficiency of 1.0% per excitation attempt. As only circular polarization is coupled into the fiber for collection along the quantization axis, we obtain the following maximally entangled atom-photon state:

$$
\begin{aligned}
|\Psi\rangle_{\text{Atom-Photon}} &= \frac{1}{\sqrt{2}}(|\downarrow\rangle_z |L\rangle + |\uparrow\rangle_z |R\rangle) \\
&= \frac{1}{\sqrt{2}}(|\downarrow\rangle_x |H\rangle + |\uparrow\rangle_x |V\rangle) \\
&= \frac{1}{\sqrt{2}}(|\downarrow\rangle_y |D\rangle + |\uparrow\rangle_y |A\rangle), \quad (1)
\end{aligned}
$$

where $|L\rangle$, $|R\rangle$, $|H\rangle$, $|V\rangle$, $|D\rangle$, and $|A\rangle$ denote left-circular ($\sigma^+$), right-circular ($\sigma^-$), horizontal, vertical, diagonal, and antidiagonal photonic polarization states, respectively, and $|\downarrow\rangle_z = |F = 1, m_F = -1\rangle$ and $|\uparrow\rangle_z = |F = 1, m_F = +1\rangle$ denote the initial qubit basis [14] [Fig. 1(c)]. The entanglement-generation cycle is repeated until a single photon is successfully coupled into a fiber and detected.

The final step is the analysis of the atom-photon entangled state. For this, the photon is registered behind a polarization analyzer, the orientation of which is defined with half- and quarter-wave plates [Fig. 1(a)]. For the atomic state readout [Fig. 1(d)], we employ a state-selective readout scheme in which the polarization $|\gamma\rangle = \cos(\alpha)|V\rangle + e^{i\phi}\sin(\alpha)|H\rangle$ of a 140 ns readout laser pulse excites atoms in the so-called bright state $|\text{Bright}\rangle = \cos(\alpha)|\downarrow\rangle_x + e^{i\phi}\sin(\alpha)|\uparrow\rangle_x$ to the $5^2P_{1/2} |F' = 1\rangle$ level. Atoms that are not transferred are referred to as dark state $|\text{Dark}\rangle = \sin(\alpha)|\downarrow\rangle_x - e^{i\phi}\cos(\alpha)|\uparrow\rangle_x$. Subsequently, the population in $5^2P_{1/2}$ is ionized by an additional laser ($\lambda = 450$ nm) and is thus released from the trap. Due to the limited lifetime of the $5^2P_{1/2}$ state, the atom can decay to the state $5^2S_{1/2} |F = 2\rangle$ before being ionized. These possible decays include errors in the readout process, which can be avoided by reexciting the atom to the state $5^2P_{3/2} |F' = 3\rangle$, where it is also ionized. Finally, the MOT beams are switched on again and the number of fluorescence photons is counted. Fluorescence counts exceeding a
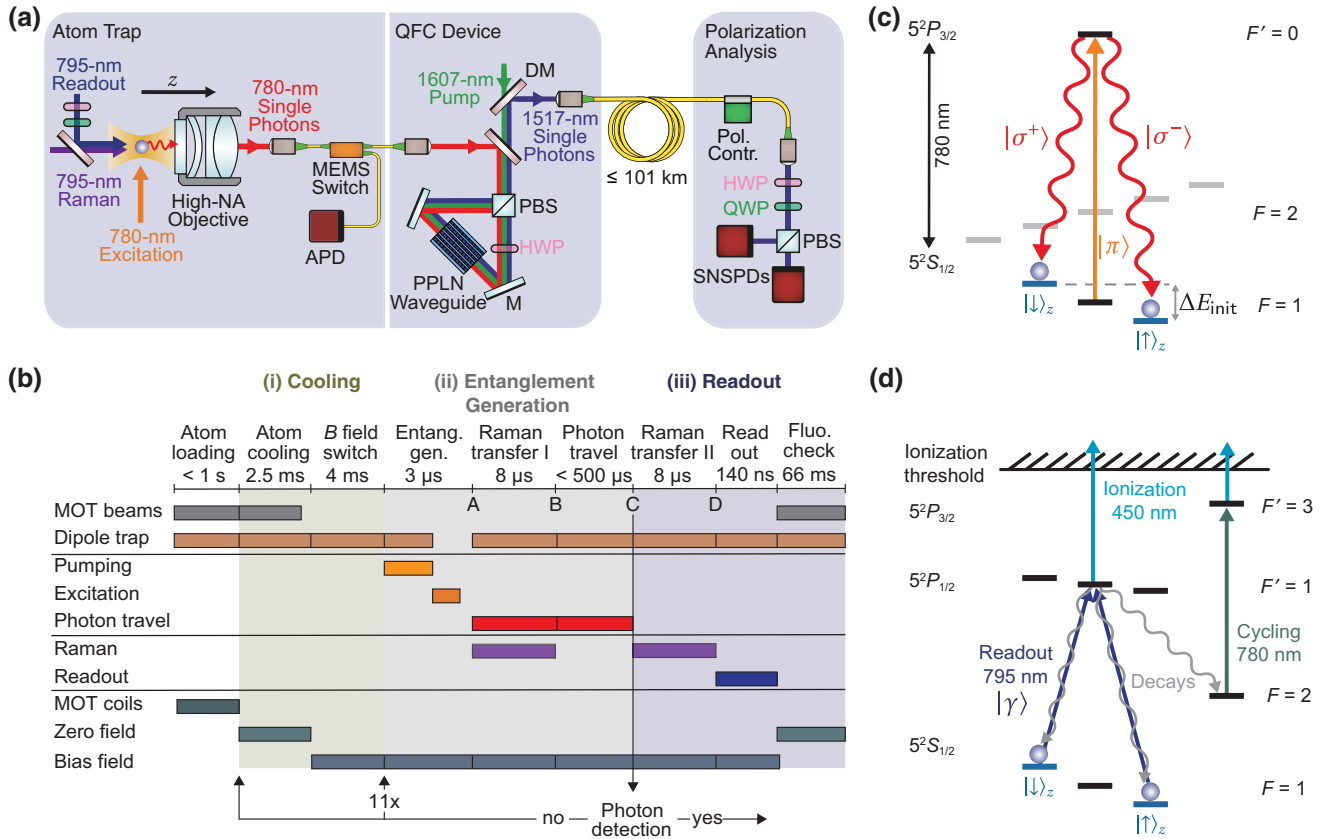
FIG. 1. The architecture of a neutral atom-based quantum network node. (a) A single $^{87}$Rb atom is stored in a strongly focused ODT (wavelength 849.5 nm, waist 2.05 μm, and trapping potential 2.3 mK for an intensity of 4.97 mW μm$^{-2}$). Emitted photons are collected by a high-numerical-aperture (NA) objective (NA = 0.5) and coupled into a 5 m single-mode fiber. The photons first pass a microelectromechanical systems (MEMS) fiber switch, which selectively guides the photons either to a silicon avalanche photodiode (APD) during atom loading and atomic state readout or to a quantum frequency-conversion (QFC) device during entanglement-generation attempts. The QFC device converts the emitted photons at 780 nm to 1517 nm. Next, the telecom photons propagate through up to 101 km of spooled fiber, after which their polarization is analyzed with a polarizing beam splitter (PBS) and superconducting nanowire single-photon detectors (SNSPDs). (b) The experimental sequence to generate and analyze atom-photon entanglement, which is divided into three stages: cooling (green background), entanglement generation (light-gray background), and atomic readout (dark-gray background). The entanglement-generation attempts are executed in bursts of 11, after which the atom is recooled. Successful detection of a single photon interrupts a burst and starts the atomic state readout. (c) The scheme of the atom-photon entanglement generation. A $\pi$-polarized laser pulse excites the atom, followed by a spontaneous decay to the $|{\downarrow}\rangle_z$ or $|{\uparrow}\rangle_z$ state. Here, $\{|{\uparrow}\rangle_z, |{\downarrow}\rangle_z\}$ is defined as the initial basis for the atomic qubit. (d) The scheme of the state-selective readout. Depending on the polarization of the readout laser pulse, i.e., $\sigma^-$, $\sigma^+$ or a superposition of them, either the state $|{\downarrow}\rangle_z$, $|{\uparrow}\rangle_z$, or a superposition of them, is initially excited to the $5^2P_{1/2}$ state and subsequently ionized. An additional cycling laser pulse reexcites the atoms, which decay to the $5^2S_{1/2}\,|F = 2\rangle$ hyperfine state during the readout process, to the $5^2P_{3/2}\,|F' = 3\rangle$ state, from which they are also ionized.

threshold (a value higher than the background counts) confirm that the atom is still present in the trap and is thus projected onto the dark state $|\mathsf{Dark}\rangle$. We define the probability of observing the atom in the trap after the readout sequence as the redetection probability $P_{\text{redetect}} \sim |\langle \Psi|\mathsf{Dark}\rangle|^2$. The fidelity of the atomic state readout is 95%.

## B. Long-lived quantum memory

The coherence time of the atomic qubit, which is defined as the time when the visibility decreases to $1/e$ of the initial value (Fig. 2; see also Appendix B), is strongly limited by two effects, when encoded in the initial basis. The first is the position-dependent dephasing caused by the ac Stark shift originating from longitudinal electric field components of the tightly focused ODT beam ($w_0 = 2.05$ μm) [44,45]. The second is due to residual magnetic field fluctuations (approximately 0.5 mG) around the atom in the laboratory environment, which result in fluctuating Zeeman shifts, causing additional dephasing. All this leads to a coherence time of hundreds of microseconds [46].
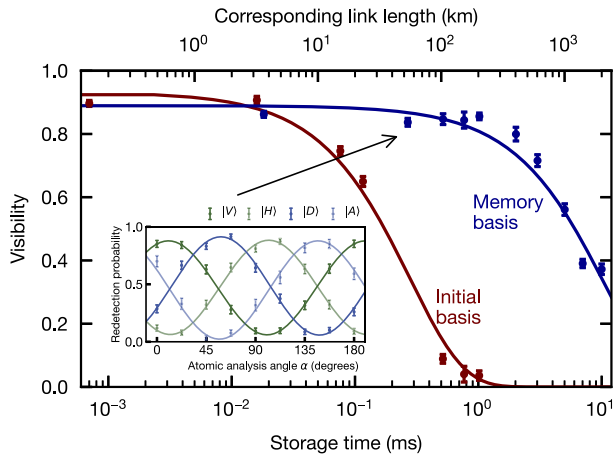
FIG. 2. Characterization of the quantum memory coherence time. The measured atom-photon state visibility as a function of the storage time (see also Appendix B). The red dots are measured visibilities in the initial basis $\{|\uparrow\rangle_z, |\downarrow\rangle_z\}$, achieved with ODT ramping and a magnetic bias field. To obtain a longer coherence time, the atomic qubit is mapped into the memory basis via a Raman transfer (blue dots). The data are fitted with exponential decay functions showing an increase in the coherence time from $279.1 \pm 31.5\,\mu$s in the initial basis to $10.51 \pm 1.04$ ms in the memory basis. The top axis indicates the corresponding fiber length by approximating the speed of the photon in the optical fiber with $\frac{2}{3}c$, where $c$ is the speed of light. The inset shows the atom-photon correlation for a storage time of about $267.92\,\mu$s.

The first effect is mitigated in two steps. Initially, the ODT intensity and thus its trap depth $U$ is adiabatically lowered from 2.3 to 0.19 mK before performing the excitation attempts. This reduces the longitudinal field components, which scale linearly with the ODT intensity [47]. The probabilities for occupying vibrational levels are preserved if the trap depth is lowered adiabatically. Therefore, the temperature should be reduced (proportional to $\sqrt{U}$) [48]. We have confirmed this by measuring the temperature of the atom via the release-and-recapture method and observing a temperature decrease from 30 $\mu$K to 8 $\mu$K [48]. The reduction in the trap depth does not necessarily improve the atomic coherence yet but it lowers the effective $\Delta B_{\text{long}}$ fields to about 6 mG. Thus, as the next step, a bias field along the $z$ axis can suppress the effects of both the residual longitudinal field components and the magnetic field fluctuations perpendicular to it. For our experiment, we have found optimal results for $B_z = 244.5$ mG. These measures result in a coherence time of $279.1 \pm 31.5\,\mu$s. Clearly, the observed time is not sufficient to maintain high fidelity for entanglement distribution over a few tens of kilometers [24].

To further increase the coherence time, we perform a transfer of the atomic qubit from the initial basis to a so-called memory basis defined by the states $\{|\downarrow\rangle_z, |F = 2, m_F = +1\rangle\}$ [42], as illustrated in Fig. 3(a).
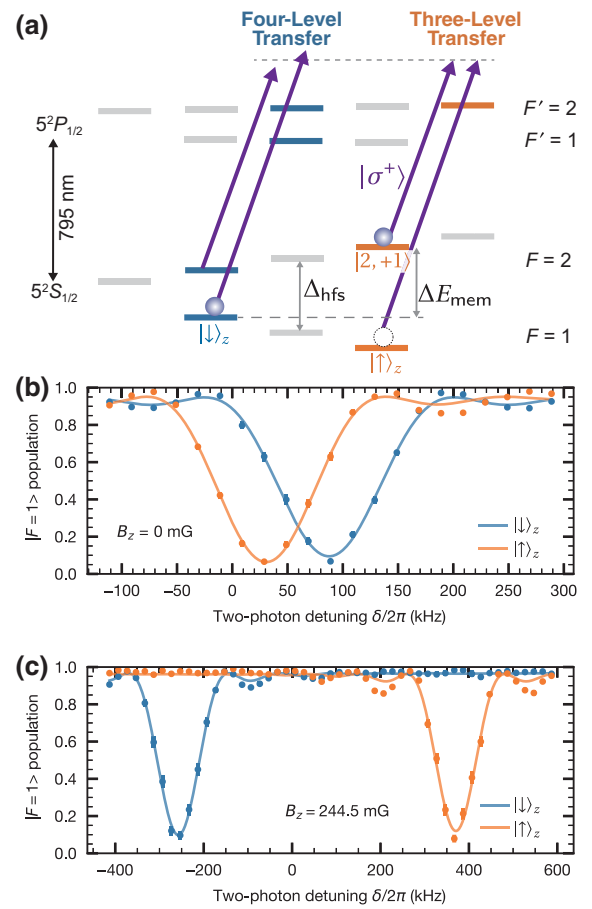


FIG. 3. Characterization of the Zeeman-state-selective Raman transfer. (a) The scheme of the Raman transfer for the atomic qubit: a Raman $\pi$ pulse, which couples either $|\uparrow\rangle_z$ to $5^2S_{1/2}\ |F = 2, m_F = +1\rangle$ or $|\downarrow\rangle_z$ to $5^2S_{1/2}\ |F = 2, m_F = -1\rangle$ via a two-photon Raman process—by choosing the former, we change from the initial basis to the memory basis $\{|\downarrow\rangle_z, |F = 2, m_F = +1\rangle\}$. (b),(c) The Raman transfer for varying two-photon detuning $\delta$ (b) at zero magnetic field and (c) with a bias field of $B_z = 244.5$ mG. An atom is prepared in the $|F = 1\rangle$ manifold in the state $|\downarrow\rangle_z$ (blue) or $|\uparrow\rangle_z$ (orange) state, after which the Raman-transfer pulse is applied. A reduced $|F = 1\rangle$ population signals a successful state transfer to the $|F = 2\rangle$ manifold. A bias field is applied to achieve a Zeeman-state-selective transfer with a contrast of $97.8 \pm 2.2\%$. This contrast is limited by the pulse power drift and the polarization purity of the Raman-transfer beam.

Ideally, in the small-field regime (the energy shifts induced by the magnetic field are small compared to the hyperfine splittings and, thus, the energy shifts are proportional to the magnetic fields), the magnetic field sensitivity of the atomic state reduces by a factor of $\chi \approx -g_F/g_I = 503$, as shown in the Supplemental Material [49]. A pair of $\sigma^+$-polarized Raman beams coherently drive the transitions between the atomic states $|\uparrow\rangle_z$ and $|F = 2, m_F = +1\rangle$ (three-level transfer) as well as between

the $|\downarrow\rangle_z$ and $|F = 2, m_F = -1\rangle$ states (four-level transfer) [see Fig. 3(a)]. To select either of the transfers with high fidelity, we compare the transfer probability with and without a bias field. For zero field [Fig. 3(b)], the optimal two-photon detuning for the transfer of $|\downarrow\rangle_z$ and $|\uparrow\rangle_z$ states differs marginally, governed solely by the differential light shift caused by the Raman beam itself. This difference is insufficient for efficient transfer and high selectivity. On the contrary, for a magnetic field of 244.5 mG along the quantization axis [Fig. 3(c)], there is a clear separation in the optimal two-photon detuning for the transfer of $|\downarrow\rangle_z$ and $|\uparrow\rangle_z$ states, allowing for the effective transfer of one of the two states while blocking the other one.

For a single-photon detuning of $2\pi \times 2.7$ GHz, we obtain an optimal $\pi$-pulse duration of 8 µs. The contrast of the Raman transfer, defined as the difference between the residual populations after a single transfer pulse when initially prepared in $|\downarrow\rangle_z$ or $|\uparrow\rangle_z$, respectively, is measured to be $97.8 \pm 2.2\%$. After a variable storage time, a second Raman pulse transfers the qubit state back to the initial basis. For this process, it is essential that the two transfer processes are coherent, thus requiring phase stability of the difference frequency of the Raman pair during the storage time, which is achieved by using a low-phase-noise microwave source referenced to a rubidium atomic clock (see Appendix A 3). Characterizing the coherence time of the atomic qubit in the memory basis, we find a coherence time of $10.51 \pm 1.04$ ms, as shown in Fig. 2 and further detailed in Appendix B. The observed increase in the coherence time is less than expected. This indicates the existence of other limiting sources contributing to atomic decoherence, most likely a differential ac Stark shift between the $|\downarrow\rangle_z$ state and $|F = 2, m_F = +1\rangle$ state in the optical dipole trap. Another factor is the effective magnetic field near the focus of the ODT beam. Despite our efforts to mitigate this by lowering the trap depth and applying a bias field, it is still challenging to completely eliminate this field. A possible solution is the implementation of a standing-wave dipole trap that mitigates the position-dependent dephasing [50]. Further, a spin-echo technique could be applied to compensate for the varying energy differences that occur during the storage time [42]. Nonetheless, the significantly longer coherence time already allows high-fidelity entanglement distribution over fiber links with a length of a few hundred kilometers.

### C. Telecom interface

For bridging long distances, it is crucial to minimize attenuation losses in the fiber links. We thus convert the emitted 780-nm single photons to the low-loss telecom S band by employing difference-frequency generation (DFG). There, the field of the single photon is combined with a strong 1607-nm pump laser field in a periodically poled lithium niobate (PPLN) waveguide,

obtaining a wavelength of 1517 nm for the converted photon [17,24]. To preserve the polarization of the single photons, the waveguide is placed in a Sagnac configuration, where the $|H\rangle$ and $|V\rangle$ polarizations are converted independently but coherently without requiring additional stabilization. Anti-Stokes Raman scattering, induced by the pump laser in the waveguide, contributes wide-band background, which is, however, strongly reduced at the pump-target wavelength difference of $\Delta\tilde{\nu} = -372.0$ cm$^{-1}$. Compared to the recent demonstration over 20 km ($\Delta\tilde{\nu}' = -317.8$ cm$^{-1}$), the Raman noise at the new wavelength combination is lower by a factor of 8 [24,51]. A spectral filter setup, including a Fabry-Perot cavity with a bandwidth of 27 MHz FWHM, reduces the QFC-induced background to 82.8 counts/s after a 50 m fiber. Altogether, an external device-conversion efficiency of up to 48% is achieved, limited by the waveguide coupling efficiency of about 81%, the transmission through optical elements (83%), the fiber-coupling efficiency (84%), and the spectral-filtering efficiency (89%). These factors reduce the high internal conversion efficiency of about 96% [17].

Lastly, the telecom photons are injected into a single-mode fiber on spools with 0.2 dB/km loss (SMF-28 Ultra) and detected by the polarization-analysis setup that contains superconducting nanowire single-photon detectors (SNSPDs) with efficiencies $\eta > 60\%$ and dark-count rates of $R_{dc} < 6$ counts/s. The experimental setup is split between two laboratories. The atomic trap setup and the QFC device are located in the first laboratory. A telecom fiber of 50-m length connects the first laboratory to the second laboratory, which houses the additional fiber spools, the spectral-filter setup, and the polarization analysis of the telecom photons.

Stress-induced birefringence in the fiber strongly influences the polarization of the photon, consequently disturbing the atom-photon entanglement. A spooled fiber is more sensitive than field-deployed fiber, since the whole spool of fiber is impacted by temperature changes. The impact of temperature changes is kept small by placing the spools in a styrofoam box inside the air-conditioned laboratory ($T \sim 20°C \pm 1.2°C$). In addition, polarization drifts in the long fiber are actively compensated by using laser light at the single-photon frequency, a fiber polarization controller, and a polarimeter together with a gradient-descent optimization algorithm [24]. Recently, different field-deployed fibers have also been carefully characterized [52–54], confirming our observation that polarization fluctuations occur on a slow time scale and can be compensated with the methods developed here.

### III. LONG-DISTANCE ENTANGLEMENT DISTRIBUTION

The performance of the quantum network node has been evaluated by analyzing the atom-photon entanglement distribution over fiber links of 50 and 101 km.
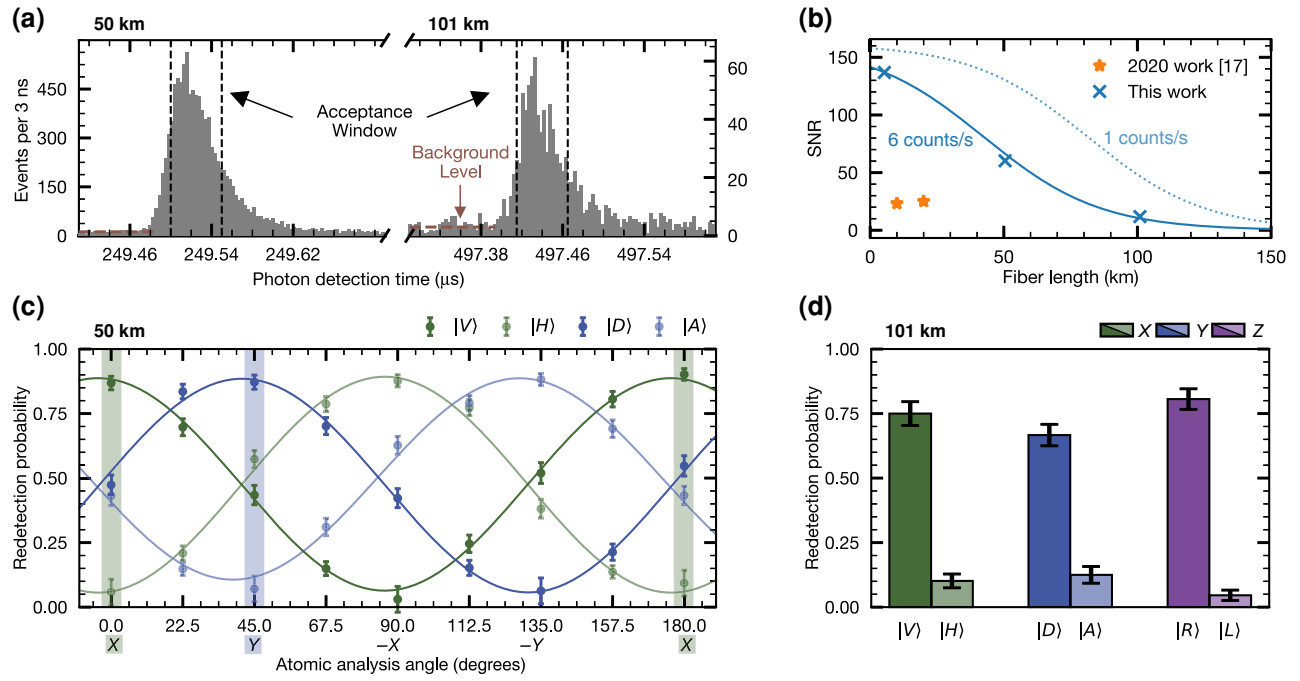
FIG. 4. The quantum network node performance for entanglement distribution over 50 and 101 km of optical fiber. (a) The detection-time histogram of the converted photons. Photon detections are accepted within a window of 50 ns, indicated with dashed black lines, accepting approximately 62 % of the single-photon events. (b) The signal-to-noise ratio (SNR) characterization as a function of the fiber length. The lines represent a model of the SNR as a function of the fiber lengths for $R_{dc} = 6$ as well as for 1 count/s. For completeness, we have also measured the SNR for a fiber length of 5 km. (c) The atom-photon state correlations over a fiber length of 50 km. In the 50-ns photon window, 6548 photon-detection events were recorded in 25.2 h. The resulting state fidelity is $\geq 84.8 \pm 1.1 \%$. (d) The atom-photon state correlations over a fiber length of 101 km. We have recorded 656 photon-detection events in 47.7 h. The atom-photon correlations have been measured in three bases, resulting in a state fidelity of $\geq 70.8 \pm 2.4 \%$. All error bars indicate one standard deviation.

In Fig. 4(a), we show the detection-time histograms of the converted photons with arrival times of 249.5 μs and 497.4 μs after the entanglement generation, respectively. Detection events consecutively trigger the atomic state readout without further substantial delay. Besides the detection of the emitted photon, there are also erroneous detection events, which consequently reduce the observed correlations and entanglement fidelity. Effectively, there are two noise sources, namely, the detector dark counts and the QFC background, the latter of which—like the signal photons—is attenuated in the fiber links. To optimize the signal-to-noise ratio (SNR) [see Fig. 4(b)] while still observing a sufficient event rate, we have applied a 50-ns photon acceptance window within the 208-ns full hard-wired window for data evaluation, accepting 62% of the detection events. This results in an observed SNR of 60.3 and 11.8 for fiber lengths of 50 and 101 km, respectively. The detector dark counts are the main noise source when extending the fiber length. A better SNR can be achieved by improving the efficiencies of the experiment and also installing low-noise detectors. For example, for $R_{dc} = 1$ count/s, the expected SNR increases to 46.7 for the same fiber length, as shown in Fig. 4(b).

In the configuration with 50-km fiber, 6548 events were recorded. At this distance, first, the attenuation in an optical fiber leads to photon loss, resulting in a tenfold signal reduction and a success probability [Eq. (C3)] of $1.09 \times 10^{-4}$. Second, an increased photon travel time leads to a repetition rate [Eq. (C2)] of 1182 Hz. Both of these factors combined yield an event rate of $1/14 \, \text{s}^{-1}$. The entanglement fidelity relative to the state $|\Psi\rangle$ has been estimated by measuring correlation probabilities in two bases. For each measured polarization state of the photon (vertical $|V\rangle$, horizontal $|H\rangle$, and diagonal $|D\rangle$, antidiagonal $|A\rangle$ linear polarization, respectively), the atomic analysis angle has been rotated from the atomic $X$ basis via $Y$, $-X$, and $-Y$ back to $X$ in steps of 22.5° [Fig. 4(c)]. The data are fitted with sinusoidal curves yielding visibilities of $82.4 \pm 1.9 \%$, $83.7 \pm 2.8 \%$, $82.8 \pm 2.8 \%$, and $78.1 \pm 2.9 \%$ for the $|V\rangle$, $|H\rangle$, $|D\rangle$, and $|A\rangle$ photon polarization states, respectively. This results in an averaged visibility of $\overline{V} = 81.8 \pm 1.3 \%$. A lower bound for the entanglement fidelity is estimated via $\mathcal{F} \geq \frac{1}{6} + \frac{5}{6}\overline{V} = 84.8 \pm 1.1 \%$, relative to the maximally entangled state. The factors of 1/6 and 5/6 emerge due to the effective $2 \times 3$ state space, as the $|F = 1, m_F = 0\rangle$ state orthogonal to $|\Psi\rangle$ can also be

populated (see Appendix E for calculating the lower bound of $\mathcal{F}$). In addition, these measurement settings also allow us to evaluate the Clauser-Horne-Shimony-Holt (CHSH) $S$ value [55]. With an $S = 2.259 \pm 0.060$, the observed atom-photon state still violates the CHSH inequality, with 4.3 standard deviations.

When distributing entanglement over a fiber length of 101 km, the success probability decreased to $1.08 \times 10^{-5}$. Due to the longer transmission time of the photon of $497\,\mu s$, the repetition rate had to be further decreased to $910\,Hz$, resulting in an event rate of only $1/262\,s^{-1}$ (see Appendix C). Generally, to estimate the entanglement fidelity, we prefer correlation measurements. because this enables not only the estimation of the fidelity but also the extraction of the CHSH $S$ value. However, for the 101-km measurement, due to an extremely low event rate, we have determined the fidelity more directly using maximal correlation points Fig. 4(d). This approach ensures the accuracy of the fidelity estimation while also reducing the number of measurement points required. It involves projecting the photonic polarization state in the eigenbasis $\{|L\rangle, |R\rangle\}$, or one of the superposition bases $\{|V\rangle, |H\rangle\}$ and $\{|D\rangle, |A\rangle\}$, while measuring the atomic qubit state in the respective orthogonal bases $X$, $Y$, or $Z$. For the correlators, we obtain $E_X = 64.8 \pm 5.3\%$, $E_Y = 54.2 \pm 5.3\%$, and $E_Z = 76.0 \pm 4.5\%$, respectively. Together, these give a lower bound on the entanglement fidelity of $\mathcal{F} \geq \frac{1}{6} + \frac{5}{6}\overline{V} = 70.8 \pm 2.4\%$, where $\overline{V} = (E_X + E_Y + E_Z)/3$ is the average visibility. This result clearly exceeds the bound of $\mathcal{F} = 50\%$ required to witness entanglement.

The decrease in the observed fidelity is attributed to the limited-SNR-induced erroneous readout, which results in uncorrelated detection events (6.6%), decoherence of the atomic state (5.0%), imperfect transfer efficiency of both Raman transfers (4.9%), imperfect atomic state readout (4.7%), entanglement-generation errors (1.1%), imperfect readout timing of the atomic state (0.8%), and experimental drift (4.0%). Note that for the achieved coherence time, no substantial decrease in fidelity is observed over up to 1 ms (see Fig. 2), which is twice the photon travel time over 101 km.

## IV. OUTLOOK

In this work, we have employed a single atom for a long-distance quantum networking experiment. Assuming that the Bell-state measurement (BSM) is located in the middle station between two single atoms 100 km apart, we can now use the results from our 50-km demonstration to estimate the fidelity of the resulting atom-atom entangled state $\mathcal{F}_{aa} \geq \frac{1}{9} + \frac{8}{9}\overline{V}_{aa}$, where $\overline{V}_{aa}$ denotes the average visibility of an atom-atom state. This visibility can be calculated as the product of the two atom-photon visibilities and the two-photon interference contrast in the BSM. For example, for a visibility of about 80% at $500\,\mu s$, considering

the travel time of the photon to the detector and the travel time of the heralding signal back for entanglement swapping, and a two-photon interference contrast in the BSM of 95.5% [24], we expect the fidelity of the entangled atom-atom state to be approximately 65%, which is higher than the threshold fidelity to perform entanglement purification [56].

Regarding the maximum atom-atom entanglement-generation rate, it can be calculated as $r_{max} = \frac{1}{2} \times \eta^2 \times R_{max}$. Here, the factor of $\frac{1}{2}$ accounts for the BSM being able to distinguish only two of the four Bell states. $\eta$ is the success probability of detecting a single photon per excitation attempt ($1.09 \times 10^{-4}$). $R_{max} = \frac{2c}{3}\frac{1}{2L}$ is the maximum repetition rate of the excitation sequence, where $\frac{2}{3}c$ is approximately the speed of light in glass fibers, and $L$ is the length from the node to the BSM. Then, the estimated probability of heralding an atom-atom entangled state over a $2 \times 50$ km distance becomes $1.2 \times 10^{-5}\,s^{-1}$. This is evidently low for a practical application and requires significant improvements in photon collection, transmission, and detection, first and foremost by implementing an optical cavity [57], which could improve this value by almost 2 orders of magnitude. However, due to the latency of receiving information of the successful photon detection, this cannot increase the rate arbitrarily, which also makes multiplexing of the entanglement-generation process inevitable. For the neutral atom platform, a promising approach is to scale up the number of atoms via the creation of (multidimensional) atom arrays [35,37] together with Rydberg [58,59] or cavity-enhanced interactions [60] between the atoms. This will allow one to realize efficient large-scale quantum networks [32].

## V. CONCLUSIONS

This experiment has not only shown the possibility of long-distance entanglement sharing but also the need for future developments in practical quantum networks. It has been possible to bridge long distances through distinct enlargement of the coherence time by employing a state-selective Raman transfer to an encoding basis much less sensitive to magnetic fields. With an increase from $200\,\mu s$ to several milliseconds, entanglement distribution can be achieved over fiber links of several hundreds of kilometers. Extending the coherence time together with efficient quantum frequency conversion is crucial for overcoming distance limitations, which previously have impeded high-efficiency and high-fidelity sharing of entanglement [17]. With this, we enlarge the distance for entanglement distribution from 20 km, with a channel loss of only 4 dB, to 101 km, with a significantly higher channel loss of 20 dB, while maintaining comparable fidelity. The next step is to develop a standing-wave optical dipole trap to mitigate rephasing effects originating from the tightly focused ODT beam, further enhancing the stability of the system.

In addition, the standing-wave configuration facilitates the simultaneous trapping of multiple single atoms, which is a key step toward a multiplexed quantum memory, with multiple qubits directly scaling up the success rate. In conclusion, this proof-of-concept experiment demonstrates a quantum network node that enables the distribution of a single photon, entangled with a single atom, over a distance of 101 km of telecom fiber spools. It provides a clear path for optimizing the achievable distance for entanglement distribution and illustrates the challenges that must be addressed on the way toward practical long-distance quantum networks.



FIG. 5. The energy-level diagram of the Raman-transfer scheme. We utilize a pair of $\sigma^+$-polarized Raman beams on the $^{87}$Rb $D_1$ line at 795-nm wavelength to employ the Raman transfer; thus two transfers are possible. For a three-level Raman transfer, we define $|m\rangle = |F = 1, m_F = +1\rangle$, $|n\rangle = |F = 2, m_F = +1\rangle$, and $|k\rangle = |F' = 2, m_{F'} = +2\rangle$. For a four-level Raman transfer, we define $|a\rangle = |F = 1, m_F = -1\rangle$, $|b\rangle = |F = 2, m_F = -1\rangle$, $|3\rangle = |F' = 1, m_{F'} = 0\rangle$, and $|4\rangle = |F' = 2, m_{F'} = 0\rangle$. We also define $|1\rangle = |F = 1, m_F = 0\rangle$ and $|2\rangle = |F = 2, m_F = 0\rangle$. The energy difference between the two levels $|1\rangle$ and $|2\rangle$ ($|3\rangle$ and $|4\rangle$) is defined as $\Delta_{\text{hfs}}$ ($\Delta_{\text{hfs'}}$). Assuming a weak bias field $B_z$, the ground (excited) levels will be split with energy difference $g_F m_F \mu_B B_z$ ($g_{F'} m_{F'} \mu_B B_z$), where $|g_F| = 1/2$ ($|g_{F'}| = 1/6$). The frequencies of the Raman pair are defined with $\omega_{\text{L1}}$ and $\omega_{\text{L2}}$, respectively.

## APPENDIX A: RAMAN-STATE TRANSFER

As presented in the main text, an essential technique is Zeeman-state-selective Raman transfer. It enables the swapping of the atomic qubit between the initial basis and the memory basis. The initial basis is used for entanglement generation and atomic state readout, whereas the memory basis, being less sensitive to magnetic field fluctuations, is used for storing the quantum state. Hence, the memory-basis encoding prolongs the atomic coherence time.

In Fig. 5, we show a schematic of the Raman-transfer scheme for $\sigma^+$ polarization. There, two different Raman-transfer processes are possible, namely, the three-level or the four-level transfer. The Hamiltonian for these processes in the rotating-wave approximation is transformed into an effective two-level system (see the Supplemental Material [49]). The detunings are defined as follows: $\Delta_l = \omega_{Ll} - \omega_{ij}$ and $\overline{\Delta} = (\Delta_1 + \Delta_2)/2$, where $\omega_{ij} = \omega_i - \omega_j$ with $l \in \{1, 2\}$ and $i, j \in \{m, n, k\}$ or $\in \{a, b, 3, 4\}$ for the three- or four-level case, respectively.

The goal is to selectively transfer only one of the two $m_F$ states to its corresponding $m_F$ state in the $F = 2$ manifold. It turns out that this is best achieved using the three-level transfer by tuning the two-photon detuning $\delta$ for a given bias field $B_z$.
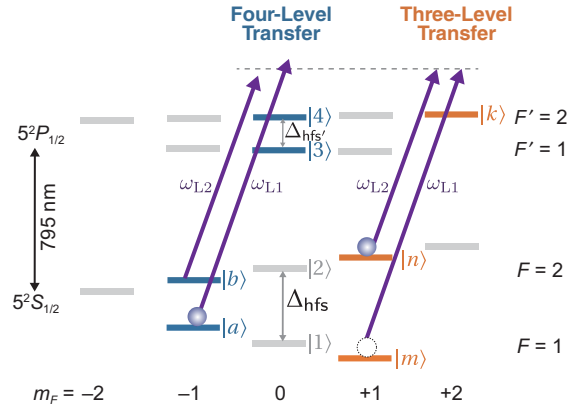
### 1. Three-level Raman transfer

In the three-level transfer scheme, the atom defined in the levels $\{|m\rangle, |n\rangle, |k\rangle\}$ interacts with two Raman beams $\{|\text{L1}\rangle, |\text{L2}\rangle\}$.

Unity state-transfer efficiency is only possible when the two diagonal items of the effective two-level Hamiltonian are equal, which results in

$$\delta_{3-\text{level}} = 2g_F \mu_B B_z/\hbar + \frac{|\Omega_{nk}|^2 - |\Omega_{mk}|^2}{4\overline{\Delta} - 8g_{F'} \mu_B B_z/\hbar}, \quad \text{(A1)}$$

where $\Omega_{ij}$ is the Rabi frequency for the corresponding transition from state $|i\rangle$ to state $|j\rangle$, $\mu_B$ is the Bohr magneton, and $g_F$ is the Landé $g$ factor.

### 2. Four-level Raman transfer

A $\sigma^+$-polarized Raman pair also enables the coherent population transfer from $|a\rangle$ to $|b\rangle$ via the two excited levels $|3\rangle$ and $|4\rangle$ in a four-level scheme. Using the same method as above, the Hamiltonian of the four-level atom $\{|a\rangle, |b\rangle, |3\rangle, |4\rangle\}$ interacting with two Raman beams $\{|\text{L1}\rangle, |\text{L2}\rangle\}$ can be written as an effective two-level Hamiltonian. Finally, to achieve optimal transfer efficiency in

this case, the detuning needs to satisfy

$$\delta_{4-\text{level}} = -2g_F\mu_B B_z/\hbar + \frac{|\Omega_{b3}|^2 - |\Omega_{a3}|^2}{4\overline{\Delta} + 4\Delta_{\text{hfs}'}}$$
$$+ \frac{|\Omega_{b4}|^2 - |\Omega_{a4}|^2}{4\overline{\Delta}}. \tag{A2}$$

### 3. Raman-state-transfer setup

A pair of 795-nm laser beams coherently drive the Raman transitions between two hyperfine states, which have a frequency difference of approximately 6.8 GHz. The beam pair is generated using a fiber-coupled electro-optical intensity modulator (NIR-MX800-LN-10, iXblue), which is temperature stabilized to better than 0.1°C. The EOM is driven by a microwave generator (SMA100B, Rohde & Schwarz) that is referenced to a rubidium atomic clock (E10-Y, Quartzlock). A bias-voltage controller (MBC-DG-LAB-B2, iXblue) locks the operating mode of the EOM to achieve a minimal carrier intensity. The power of the Raman-beam pair is actively stabilized using a proportional-integral-differential (PID) controller (STEM-lab 125-14, Redpitaya), achieving a residual power drift of less than 1.4%.

## APPENDIX B: COHERENCE-TIME CHARACTERIZATION

The coherence time of the single-atom quantum state is limited mainly by two factors: the residual magnetic field noise (Gaussian distribution, $\Delta B_{x,y,z} \sim 0.5\,\text{mG}$) and the position-dependent longitudinal field components along the $y$ axis caused by the strongly focused ODT ($\Delta B_{\text{long}}$ [44]). Neither of these destroys the coherence of the quantum state due to the interaction with an environment but, rather, causes dephasing, i.e., a random phase for every single observation. This can be best seen by considering the effect of the ODT. After averaging over many runs, the visibility of a correlation measurement drops on a short time scale but refocuses after a time equal to the transverse oscillation period of the trap [61], in this experiment after 13.7 µs.

To characterize the atomic coherence time, we measure atom-photon correlations as a function of the storage time of the atom (in multiples of the trap period). The storage time is defined as the time delay between the generation of atom-photon entanglement and the state readout, commonly referred to as readout delay, as illustrated in the time sequence between A and D in Fig. 1. For example, to determine the coherence time of the atomic qubit in the memory basis, the atomic state is first transferred to the memory basis after the emission of the photon and then allowed to evolve freely over a set delay time. Finally, the atomic qubit is coherently transferred back to the initial basis before the readout is performed. To analyze the
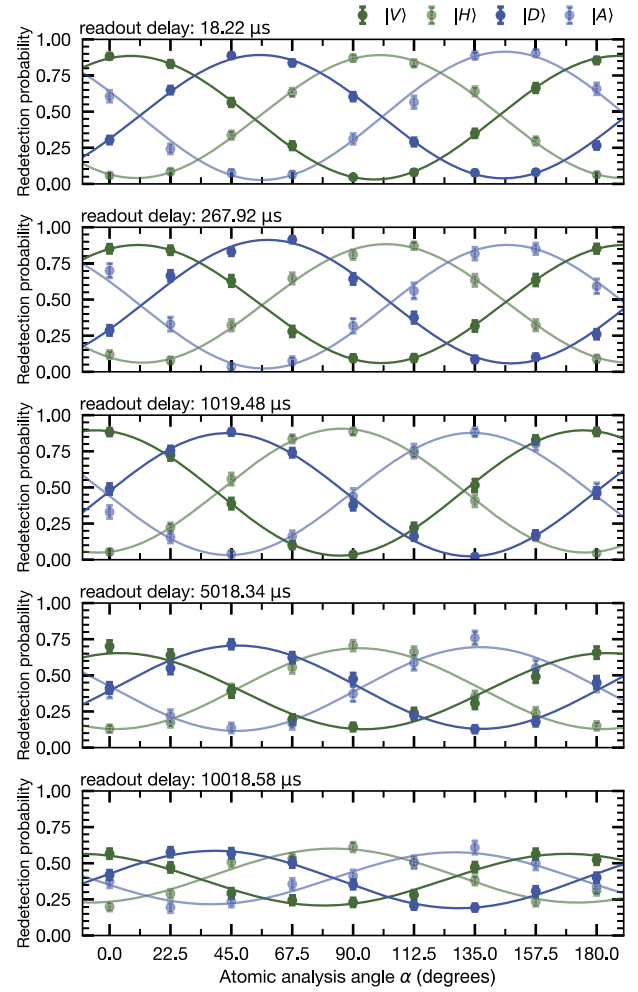


FIG. 6. An analysis of the quantum memory coherence time in the memory basis by measuring atom-photon correlations at different storage times.

entanglement, we project the photonic state onto the $\hat{\sigma}_x$-basis $\{|H\rangle, |V\rangle\}$ and the $\hat{\sigma}_y$ basis $\{|D\rangle, |A\rangle\}$ while rotating the atomic readout basis by changing the polarization of the readout laser. For each time delay, by individually fitting sinusoidal functions to the data from each correlation fringe, we can obtain the visibility (peak-to-peak amplitude), as depicted in Fig. 6. These values are used to visualize the decay of the coherence in Fig. 7.

Starting with the observation of the state with the atom in the ODT at trap depths of 2.3 mK, without any further measures at all (Fig. 7(a), light-gray curve), yields a coherence time of $194.3 \pm 32.6\,\mu\text{s}$. Lowering the trap depth to 0.19 mK should, correspondingly, lower the effective $\Delta B_{\text{long}}$ and the atomic temperature. However, it also results in an increased uncertainty in the atomic position, which over the then longer oscillation period leads to the same dephasing effect. The observed coherence time of $184.9 \pm 20.7\,\mu\text{s}$ (Fig. 7(b), black curve) indicates
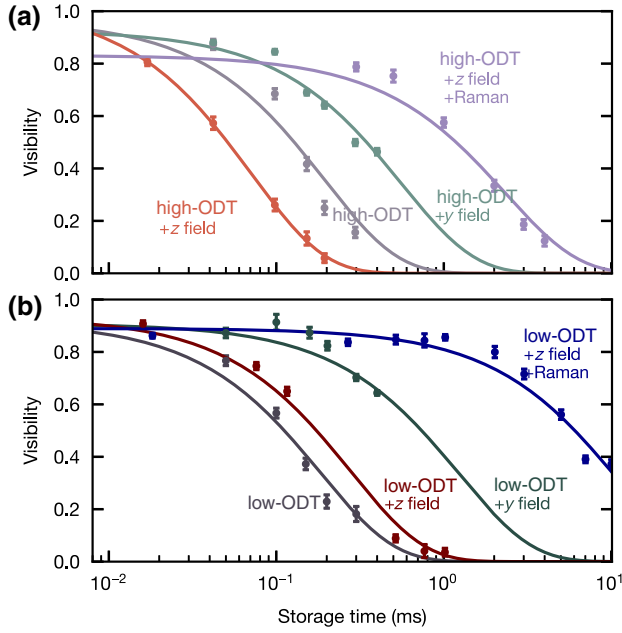
FIG. 7. The optimization of the quantum memory coherence time. During the storage time, two sets of dipole trap depths are used to determine the coherence time under different conditions. (a) The dipole trap depth is 2.3 mK (referred to as "high-ODT"). For these measurements, four different conditions have been tested: high ODT (light gray), a bias field along the $y$ axis of $B_y$=64 mG (light green), a bias field along the $z$ axis of $B_z$=244.5 mG (light red), and a Raman transfer to the memory basis together with a bias field of $B_z$=244.5 mG (light blue), respectively. The corresponding coherence times for these four conditions are $194.3 \pm 32.6 \,\mu s$, $560.2 \pm 67.3 \,\mu s$, $71.4 \pm 1.6 \,\mu s$, and $2.32 \pm 0.37$ ms, respectively. (b) The dipole trap depth is adiabatically ramped down to 0.19 mK (referred to as "low-ODT") and the same conditions yield coherence times of $184.9 \pm 20.7 \,\mu s$, $1.24 \pm 0.18$ ms, $279.1 \pm 31.5 \,\mu s$, and $10.51 \pm 1.04$ ms, respectively.

that merely reducing the trap depth does not improve the atomic coherence.

A magnetic bias field can play a crucial role in guiding the atomic evolution in the optical dipole trap. By applying a sufficiently strong magnetic field in one direction, field fluctuations perpendicular to this field can be suppressed. For instance, applying a bias field $B_y$ along the $y$ axis can reduce the impact of field fluctuations on the atomic state from two directions ($\Delta B_x$ and $\Delta B_z$). Thus, only $y$-axis field fluctuations will affect the evolution of the atomic state. Therefore, with a $B_y$ bias field of 65 mG, we suppress magnetic field fluctuations and drifts along the $x$ and $z$ axes. Although the longitudinal field components of the ODT are not suppressed, we still achieve an extended coherence time of $560.2 \pm 67.3 \,\mu s$, as shown by the light green curve in Fig. 7(a).

In contrast, a bias field $B_z$ along the $z$ axis, set at 244.5 mG, results in a shorter coherence time, as depicted

by the light-red curve in Fig. 7(a). This is because, at trap depth $U = 2.3$ mK ($T = 30 \,\mu K$), the atom experiences fluctuations of the effective $\Delta B_{\text{long}}$ fields of approximately 45 mG. Since the bias field is of the same order of magnitude, the atomic state is influenced by the fluctuations of both. Coherence can be maintained for only $71.4 \pm 1.6 \,\mu s$. There are two possibilities to address this problem. The first is to increase $B_z$ significantly, to a few gauss, even to a "magic magnetic field" of 3.2 G. The other is to reduce the longitudinal field components by lowering the trap depth. The first approach, while effective, also causes fast Larmor precession, requiring that the readout process of the atomic state has to be performed faster than that period. This is not possible with the current experimental control. The second approach, adiabatically lowering the trap depth to 0.19 mK, reduces $\Delta B_{\text{long}}$ to approximately 6 mG, which is now about 2 orders of magnitude lower than the bias field of 244.5 mG, thus enabling us to suppress these field fluctuations. Indeed, this results in a coherence time of $279.1 \pm 31.5 \,\mu s$ [dark-red curve in Fig. 7(b)]. This leaves compensating for the field fluctuations along the $z$ direction as the final challenge to be addressed. Raman-state transfer into a basis less sensitive to the magnetic field finally gives an atomic coherence time of $10.51 \pm 1.04$ ms [dark-blue curve in Fig. 7(b)], sufficient for entanglement sharing over a few hundreds of kilometers.

## APPENDIX C: ENTANGLEMENT GENERATION RATE

The atom-photon entanglement-generation rate $r$ in the experiment is given by

$$r = \phi R_{\text{exp}} \eta, \qquad (C1)$$

where $\phi$ is the duty cycle of the experiment, $R_{\text{exp}}$ is the repetition rate of the entanglement-generation attempts, and $\eta$ denotes the success probability of detecting a photon for each entanglement-generation attempt.

The average repetition rate $R_{\text{exp}}$ is

$$R_{\text{exp}}(L) = \frac{1}{T(L)} = \frac{1}{T(0) + L/c_f}, \qquad (C2)$$

where $T(L)$ is the duration of an entanglement-generation attempt, $L$ is the fiber length, and $c_f$ is the speed of light in the optical fiber, which is, to a good approximation, about $\frac{2}{3}c \approx 200000 \text{ km s}^{-1}$. $T(0)$ is the time of an entanglement-generation attempt for a link with $L = 0$. It includes the preparation of the initial qubit state (3 μs), the generation of the entanglement (200 ns), the duration of Raman transfer (8 μs), and the time to cool the atom and magnetic field stabilization per excitation attempt (6.5 ms/11), resulting in $T(0) = 602.12 \,\mu s$. In this work, we have thus used repetition rates of 1.59 , 1.18 , and 0.91 kHz for fiber lengths of

5, 50, and 101 km, which are limited by the travel time of the photon through the optical fiber and the switching time of the magnetic field from zero field to magnetic guiding field (4 ms), both of which can be optimized independently for future work.

The success probability of generating, propagating, and detecting a single photon at 1517 nm for each entanglement-generation attempt equals

$$\eta(L) = \eta(0)e^{-\frac{\alpha}{10}L}, \tag{C3}$$

where $\eta(0)$ is the success probability with $L = 0$ and $\alpha$ is the attenuation coefficient in the telecom fiber. Here, $\eta(0)$ includes the collection and coupling efficiencies of the single photons emitted by the single atoms per excitation attempt (1.0%), the transmission of the microelectromechanical systems (MEMS) switch (85%), the total efficiency of the QFC setup (48%, not optimally aligned), the transmission efficiency of the single photon through a filter cavity (82%), the transmission efficiency of the photon projection setup and fiber coupling (85%), the three fiber-fiber connectors (94%) and the average detection efficiency of the SNSPDs (59.7%). Using QFC, the attenuation rate is reduced to 0.2 dB km$^{-1}$ at 1517 nm, such that we obtain a transmission of 1.0% when photons travel through the 101-km fiber. The obtained success probabilities for the different fiber lengths within an acceptance photon window of 50 ns are listed in Table I.

The duty cycle is approximately 1/2 in the experiment, including the time required for the polarization compensation of the long fibers, the magnetic field stabilization, the Raman pulse power stabilization, and the time used for verifying whether or not an atom is present in the trap.

In the full hard-wired acceptance window (208 ns), we have recorded 11 939, 9983, and 1058 events within 5.8, 25.2, and 47.4 h for fiber-link lengths of 5, 50, and 101 km, respectively, resulting in event rates of 1/2 $s^{-1}$, 1/9 $s^{-1}$, and 1/162 $s^{-1}$, respectively, for coincidence detection. The obtained event rates in the 50-ns acceptance window are listed in Table I.

TABLE I. The observed entanglement-generation success probabilities and rates. The observed success probabilities of generating atom-photon entanglement ($\eta$) and the entanglement-generation rate ($r$), for the different fiber-link lengths $L$, are listed. The success probabilities contain only photon-detection events in the 50-ns acceptance window.

| $L$ (km) | $\eta$ | $r$ ($s^{-1}$) |
|---|---|---|
| 5 | $0.8277 \times 10^{-3}$ | 1/3 |
| 50 | $0.109 \times 10^{-3}$ | 1/14 |
| 101 | $0.0108 \times 10^{-3}$ | 1/262 |

## APPENDIX D: SIGNAL- AND NOISE-DETECTION EVENTS

The entanglement observable between an atom and a photon is easily degraded by various noise sources. To address this, we have first conducted a detailed analysis on the selection of the photon acceptance window using data from the 101-km atom-photon experiment (Fig. 8). By fixing the start timing and varying the end timing of the acceptance window, we have observed its effect on the SNR, the fidelity, and the number of events. This shows that while increasing the acceptance-window length leads to a higher number of events, it also results in a reduced SNR and fidelity. Specifically, with a 50-ns interval, approximately 62% of the events are detected. Taking into account the uniform distribution of the QFC background and the detector dark counts, time filtering is expected to improve the SNR by a factor of $62\% \times (208\,\text{ns}/50\,\text{ns}) = 2.6$. Indeed, the SNR has been measured at 11.8 for the 50 ns window, whereas at 160 ns, the SNR dropped to 5.2, making a 2.3-fold improvement as expected. Therefore, we opted for an acceptance-window length of 50 ns to balance the high SNR and fidelity with sufficient event counts.

To further increase the percentage of detection events, approaches involve the implementation of lower-noise detectors and the reduction of the QFC background by, e.g., utilizing the pump-target wavelengths at 1610–1513 nm ($\Delta\tilde{\nu}' = -398.2\,\text{cm}^{-1}$).
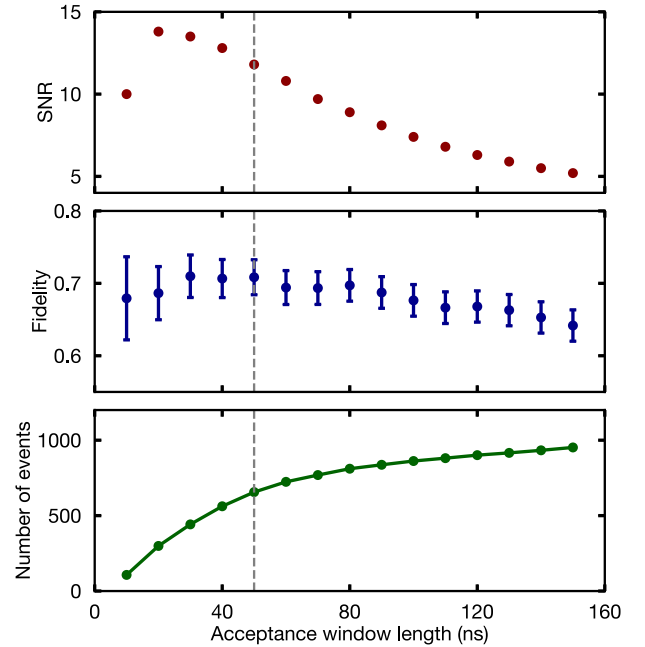


FIG. 8. An analysis of the data recorded during the 101-km atom-photon experiment: the effects of time filtering on the SNR, the fidelity, and the number of events. The length of the acceptance window is varied by fixing the start timing of the acceptance window and changing the end timing.
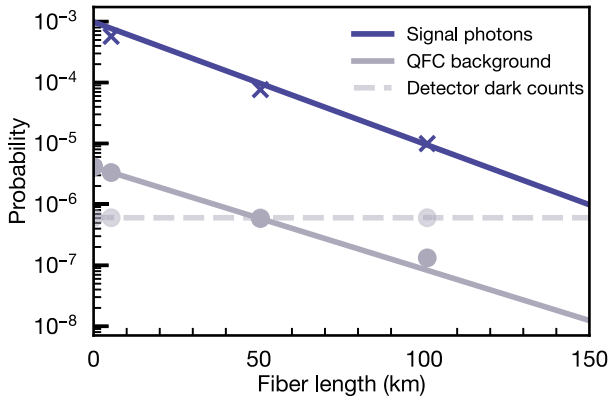
FIG. 9. The detector-click probabilities for varying fiber length. Three processes can be distinguished that generate single-photon detector clicks: the signal photons (blue), noise introduced by the QFC device (gray solid line), and noise introduced by the detectors, i.e., detector dark counts (gray dashed line). In our setup, the detector dark counts become the prominent noise source for fiber lengths above 50 km.

With this 50-ns photon window, we have then analyzed the probability of detecting a single photon, a background originating in the QFC process, and the detector dark counts. Like the single photons, the background from the QFC propagates in the optical fiber and is thus also attenuated (approximately 0.2 dB/km). Therefore, in our setup, for fiber lengths significantly longer than 50 km, the dark counts of the detectors, which are not dependent on the fiber length, become the primary noise source, as shown in Fig. 9. As mentioned in the main text, the next step for long-distance entanglement distribution requires further improvements of the photon collection as well as very low-noise single-photon detectors without sacrificing the detection efficiency.

## APPENDIX E: ATOM-PHOTON FIDELITY

For extracting fidelities from the measured visibilities, one must take into consideration that the $5^2 S_{1/2} \, |F = 1\rangle$ state of the $^{87}$Rb atom is a spin-1 system. Although the atomic qubit is encoded in the state $|F = 1, m_F = \pm 1\rangle$, atomic state evolution due to magnetic field noise in the $x$ or $y$ axis (the quantization axis is the $z$ axis) can lead to a population in the third spin state $|F = 1, m_F = 0\rangle$ [46]. Therefore, the atom-photon state resides in the $3 \times 2$ space spanned by $\{|\downarrow\rangle_z, |F = 1, m_F = 0\rangle, |\uparrow\rangle_z\}$, and $\{|R\rangle, |L\rangle\}$.

For a pure state, the density matrix is defined as $\hat{\rho} = |\Psi\rangle\langle\Psi|$, while for a completely mixed state, the density matrix is given by $\hat{\rho} = \frac{1}{6}\hat{\mathbb{I}}$. Therefore, under the assumption of isotropic dephasing toward white noise, the density matrix of a maximally entangled atom-photon state can be expressed as

$$\hat{\rho} = \bar{V}|\Psi\rangle\langle\Psi| + \left(1 - \bar{V}\right)\frac{1}{6}\hat{\mathbb{I}}, \tag{E1}$$

where $\bar{V}$ is the mean visibility. Given the state represented by the density matrix $\hat{\rho}$ from Eq (E1), the lower bound of the probability of observing the atom-photon state in the pure state $|\Psi\rangle$, also referred to as the fidelity $\mathcal{F}$, can be determined as follows:

$$\mathcal{F} \geq \langle\Psi|\hat{\rho}|\Psi\rangle = \frac{1}{6} + \frac{5}{6}\bar{V}. \tag{E2}$$

This approach differs from the commonly used method for estimating the fidelity in an entangled two-qubit state, where the fidelity is calculated as $\mathcal{F} = \frac{1}{4} + \frac{3}{4}\bar{V}$, based on the state space spanned by $\{|\downarrow\rangle_z, |\uparrow\rangle_z\}$ and $\{|R\rangle, |L\rangle\}$. However, in our case, this formula would yield a higher fidelity, leading to an overestimation of the fidelity of the generated atom-photon state.

The fidelity of the atom-photon state that we have prepared is mainly affected by off-resonant excitations, which result from imperfect optical pumping and polarization errors of the excitation light. During the detection process, several factors such as off-resonant excitation of the dark state or polarization errors of the readout laser, contribute to the limited fidelity (for detailed discussions, see Refs. [62,63]).

[1] S. Wehner, D. Elkouss, and R. Hanson, Quantum Internet: A vision for the road ahead, Science **362**, eaam9288 (2018).

[2] C. Monroe, R. Raussendorf, A. Ruthven, K. R. Brown, P. Maunz, L.-M. Duan, and J. Kim, Large-scale modular quantum-computer architecture with atomic memory and photonic interconnects, Phys. Rev. A **89**, 022317 (2014).

[3] D. Cuomo, M. Caleffi, and A. S. Cacciapuoti, Towards a distributed quantum computing ecosystem, IET Quantum Commun. **1**, 3 (2020).

[4] A. Acín, N. Brunner, N. Gisin, S. Massar, S. Pironio, and V. Scarani, Device-independent security of quantum cryptography against collective attacks, Phys. Rev. Lett. **98**, 230501 (2007).

[5] D. P. Nadlinger, P. Drmota, B. C. Nichol, G. Araneda, D. Main, R. Srinivas, D. M. Lucas, C. J. Ballance, K. Ivanov, E. Y. Z. Tan, P. Sekatski, R. L. Urbanke, R. Renner, N. Sangouard, and J. D. Bancal, Experimental quantum key distribution certified by Bell's theorem, Nature **607**, 682 (2022).

[6] W. Zhang, T. van Leent, K. Redeker, R. Garthoff, R. Schwonnek, F. Fertig, S. Eppelt, W. Rosenfeld, V. Scarani, C. C. W. Lim, and H. Weinfurter, A device-independent quantum key distribution system for distant users, Nature **607**, 687 (2022).

[7] T. J. Proctor, P. A. Knott, and J. A. Dunningham, Multiparameter estimation in networked quantum sensors, Phys. Rev. Lett. **120**, 080501 (2018).

[8] E. T. Khabiboulline, J. Borregaard, K. De Greve, and M. D. Lukin, Optical interferometry with quantum networks, Phys. Rev. Lett. **123**, 070504 (2019).

[9] J. Yin, Y.-H. Li, S.-K. Liao, M. Yang, Y. Cao, L. Zhang, J.-G. Ren, W.-Q. Cai, W.-Y. Liu, S.-L. Li, R. Shu, Y.-M. Huang, L. Deng, L. Li, Q. Zhang, N.-L. Liu, Y.-A. Chen, C.-Y. Lu, X.-B. Wang, F. Xu, J.-Y. Wang, C.-Z. Peng, A. K. Ekert, and J.-W. Pan, Entanglement-based secure quantum cryptography over 1,120 kilometres, Nature **582**, 501 (2020).

[10] S. P. Neumann, A. Buchner, L. Bulla, M. Bohmann, and R. Ursin, Continuous entanglement distribution over a transnational 248 km fiber link, Nat. Commun. **13**, 6134 (2022).

[11] H.-J. Briegel, W. Dür, J. I. Cirac, and P. Zoller, Quantum repeaters: The role of imperfect local operations in quantum communication, Phys. Rev. Lett. **81**, 5932 (1998).

[12] P. van Loock, W. Alt, C. Becher, O. Benson, H. Boche, C. Deppe, J. Eschner, S. Höfling, D. Meschede, P. Michler, F. Schmidt, and H. Weinfurter, Extending quantum links: Modules for fiber-and memory-based quantum repeaters, Adv. Quantum Technol. **3**, 1900141 (2020).

[13] B. B. Blinov, D. L. Moehring, L. M. Duan, and C. Monroe, Observation of entanglement between a single trapped atom and a single photon, Nature **428**, 153 (2004).

[14] J. Volz, M. Weber, D. Schlenk, W. Rosenfeld, J. Vrana, K. Saucke, C. Kurtsiefer, and H. Weinfurter, Observation of entanglement of a single photon with a trapped atom, Phys. Rev. Lett. **96**, 030404 (2006).

[15] V. Krutyanskiy, M. Meraner, J. Schupp, V. Krcmarsky, H. Hainzer, and B. Lanyon, Light-matter entanglement over 50 km of optical fibre, npj Quantum Inf. **5**, 27 (2019).

[16] Y. Yu, F. Ma, X.-Y. Luo, B. Jing, P.-F. Sun, R.-Z. Fang, C.-W. Yang, H. Liu, M.-Y. Zheng, X.-P. Xie, W.-J. Zhang, L.-X. You, Z. Wang, T.-Y. Chen, Q. Zhang, X.-H. Bao, and J.-W. Pan, Entanglement of two quantum memories via fibres over dozens of kilometres, Nature **578**, 240 (2020).

[17] T. van Leent, M. Bock, R. Garthoff, K. Redeker, W. Zhang, T. Bauer, W. Rosenfeld, C. Becher, and H. Weinfurter, Long-distance distribution of atom-photon entanglement at telecom wavelength, Phys. Rev. Lett. **124**, 010510 (2020).

[18] E. Bersin, M. Sutula, Y. Q. Huan, A. Suleymanzade, D. R. Assumpcao, Y.-C. Wei, P.-J. Stas, C. M. Knaut, E. N. Knall, C. Langrock, N. Sinclair, R. Murphy, R. Riedinger, M. Yeh, C. J. Xin, S. Bandyopadhyay, D. D. Sukachev, B. Machielse, D. S. Levonian, M. K. Bhaskar, S. Hamilton, H. Park, M. Lončar, M. M. Fejer, P. B. Dixon, D. R. Englund, and M. D. Lukin, Telecom networking with a diamond quantum memory, PRX Quantum **5**, 010303 (2024).

[19] L. J. Stephenson, D. P. Nadlinger, B. C. Nichol, S. An, P. Drmota, T. G. Ballance, K. Thirumalai, J. F. Goodwin, D. M. Lucas, and C. J. Ballance, High-rate, high-fidelity entanglement of qubits across an elementary quantum network, Phys. Rev. Lett. **124**, 110501 (2020).

[20] S. Langenfeld, S. Welte, L. Hartung, S. Daiss, P. Thomas, O. Morin, E. Distante, and G. Rempe, Quantum teleportation between remote qubit memories with only a single photon as a resource, Phys. Rev. Lett. **126**, 130502 (2021).

[21] V. Krutyanskiy, M. Galli, V. Krcmarsky, S. Baier, D. A. Fioretto, Y. Pu, A. Mazloom, P. Sekatski, M. Canteri, M. Teller, J. Schupp, J. Bate, M. Meraner, N. Sangouard, B. Lanyon, and T. E. Northup, Entanglement of trapped-ion qubits separated by 230 meters, Phys. Rev. Lett. **130**, 050803 (2023).

[22] X. Liu, J. Hu, Z.-F. Li, X. Li, P.-Y. Li, P.-J. Liang, Z.-Q. Zhou, C.-F. Li, and G.-C. Guo, Heralded entanglement distribution between two absorptive quantum memories, Nature **594**, 41 (2021).

[23] D. Lago-Rivera, S. Grandi, J. V. Rakonjac, A. Seri, and H. de Riedmatten, Telecom-heralded entanglement between multimode solid-state quantum memories, Nature **594**, 37 (2021).

[24] T. van Leent, M. Bock, F. Fertig, R. Garthoff, S. Eppelt, Y. Zhou, P. Malik, M. Seubert, T. Bauer, W. Rosenfeld, W. Zhang, C. Becher, and H. Weinfurter, Entangling single atoms over 33 km telecom fibre, Nature **607**, 69 (2022).

[25] X.-Y. Luo, Y. Yu, J.-L. Liu, M.-Y. Zheng, C.-Y. Wang, B. Wang, J. Li, X. Jiang, X.-P. Xie, Q. Zhang, X.-H. Bao, and J.-W. Pan, Postselected entanglement between two atomic ensembles separated by 12.5 km, Phys. Rev. Lett. **129**, 050503 (2022).

[26] C. M. Knaut, A. Suleymanzade, Y.-C. Wei, D. R. Assumpcao, P.-J. Stas, Y. Q. Huan, B. Machielse, E. N. Knall, M. Sutula, G. Baranes, N. Sinclair, C. De-Eknamkul, D. S. Levonian, M. K. Bhaskar, H. Park, M. Lončar, and M. D. Lukin, Entanglement of nanophotonic quantum memory nodes in a telecommunication network, arXiv Preprint arXiv:2310.01316 (2023).

[27] M. Pompili, S. L. N. Hermans, S. Baier, H. K. C. Beukers, P. C. Humphreys, R. N. Schouten, R. F. L. Vermeulen, M. J. Tiggelman, L. dos Santos Martins, B. Dirkse, S. Wehner, and R. Hanson, Realization of a multinode quantum network of remote solid-state qubits, Science **372**, 259 (2021).

[28] S. Hermans, M. Pompili, H. Beukers, S. Baier, J. Borregaard, and R. Hanson, Qubit teleportation between non-neighbouring nodes in a quantum network, Nature **605**, 663 (2022).

[29] M. K. Bhaskar, R. Riedinger, B. Machielse, D. S. Levonian, C. T. Nguyen, E. N. Knall, H. Park, D. Englund, M. Lončar, D. D. Sukachev, and M. D. Lukin, Experimental demonstration of memory-enhanced quantum communication, Nature **580**, 60 (2020).

[30] S. Langenfeld, P. Thomas, O. Morin, and G. Rempe, Quantum repeater node demonstrating unconditionally secure key distribution, Phys. Rev. Lett. **126**, 230506 (2021).

[31] V. Krutyanskiy, M. Canteri, M. Meraner, J. Bate, V. Krcmarsky, J. Schupp, N. Sangouard, and B. P. Lanyon, Telecom-wavelength quantum repeater node based on a trapped-ion processor, Phys. Rev. Lett. **130**, 213601 (2023).

[32] J. P. Covey, H. Weinfurter, and H. Bernien, Quantum networks with neutral atom processing nodes, npj Quantum Inf. **9**, 90 (2023).

[33] M. Brekenfeld, D. Niemietz, J. D. Christesen, and G. Rempe, A quantum network node with crossed optical fibre cavities, Nat. Phys. **16**, 647 (2020).

[34] K. Barnes, P. Battaglino, B. J. Bloom, K. Cassella, R. Coxe, N. Crisosto, J. P. King, S. S. Kondov, K. Kotru, S. C. Larsen, J. Lauigan, B. J. Lester, M. McDonald, E. Megidish, S. Narayanaswami, C. Nishiguchi, R. Notermans, L. S. Peng, A. Ryou, T.-Y. Wu, and M. Yarwood,

Assembly and coherent control of a register of nuclear spin qubits, Nat. Commun. **13**, 2779 (2022).

[35] D. Bluvstein, H. Levine, G. Semeghini, T. T. Wang, S. Ebadi, M. Kalinowski, A. Keesling, N. Maskara, H. Pichler, M. Greiner, V. Vuletić, and M. D. Lukin, A quantum processor based on coherent transport of entangled atom arrays, Nature **604**, 451 (2022).

[36] P. Scholl, M. Schuler, H. J. Williams, A. A. Eberharter, D. Barredo, K.-N. Schymik, V. Lienhard, L.-P. Henry, T. C. Lang, T. Lahaye, A. M. Läuchli, and A. Browaeys, Quantum simulation of 2D antiferromagnets with hundreds of Rydberg atoms, Nature **595**, 233 (2021).

[37] I. S. Madjarov, J. P. Covey, A. L. Shaw, J. Choi, A. Kale, A. Cooper, H. Pichler, V. Schkolnik, J. R. Williams, and M. Endres, High-fidelity entanglement and detection of alkaline-earth Rydberg atoms, Nat. Phys. **16**, 857 (2020).

[38] S. J. Evered, D. Bluvstein, M. Kalinowski, S. Ebadi, T. Manovitz, H. Zhou, S. H. Li, A. A. Geim, T. T. Wang, N. Maskara, H. Levine, G. Semeghini, M. Greiner, V. Vuletić, and M. D. Lukin, High-fidelity parallel entangling gates on a neutral-atom quantum computer, Nature **622**, 268 (2023).

[39] A. Gritsch, L. Weiss, J. Früh, S. Rinner, and A. Reiserer, Narrow optical transitions in erbium-implanted silicon waveguides, Phys. Rev. X **12**, 041009 (2022).

[40] R. Ikuta, T. Kobayashi, T. Kawakami, S. Miki, M. Yabuno, T. Yamashita, H. Terai, M. Koashi, T. Mukai, T. Yamamoto, and N. Imoto, Polarization insensitive frequency conversion for an atom-photon entanglement distribution via a telecom network, Nat. Commun. **9**, 1997 (2018).

[41] M. Bock, P. Eich, S. Kucera, M. Kreis, A. Lenhard, C. Becher, and J. Eschner, High-fidelity entanglement between a trapped ion and a telecom photon via quantum frequency conversion, Nat. Commun. **9**, 1998 (2018).

[42] M. Körber, O. Morin, S. Langenfeld, A. Neuzner, S. Ritter, and G. Rempe, Decoherence-protected memory for a single-photon qubit, Nat. Photonics **12**, 18 (2018).

[43] K. Redeker, PhD thesis, Ludwig-Maximilians-Universität München, 2020.

[44] W. Rosenfeld, Ph.D. thesis, Ludwig-Maximilians-Universität München, 2008.

[45] J. D. Thompson, T. G. Tiecke, A. S. Zibrov, V. Vuletic, and M. D. Lukin, Coherence and Raman sideband cooling of a single atom in an optical tweezer, Phys. Rev. Lett. **110**, 133001 (2013).

[46] W. Rosenfeld, J. Volz, M. Weber, and H. Weinfurter, Coherence of a qubit stored in Zeeman levels of a single optically trapped atom, Phys. Rev. A **84**, 022343 (2011).

[47] S. Kuhr, W. Alt, D. Schrader, I. Dotsenko, Y. Miroshnychenko, A. Rauschenbeutel, and D. Meschede, Analysis of dephasing mechanisms in a standing-wave dipole trap, Phys. Rev. A **72**, 023406 (2005).

[48] C. Tuchendler, A. M. Lance, A. Browaeys, Y. R. P. Sortais, and P. Grangier, Energy distribution and cooling of a single atom in an optical tweezer, Phys. Rev. A **78**, 033425 (2008).

[49] See the Supplemental Material at http://link.aps.org/supplemental/10.1103/PRXQuantum.5.020307, for further details on the calculation of Raman-state transfer and the magnetic field sensitivity of the memory basis.

[50] D. Taray, Master thesis, Ludwig-Maximilians-Universität München, Germany, 2020.

[51] T. van Leent, Ph.D. thesis, Ludwig-Maximilians-Universität München, Germany, 2023.

[52] Y. Shi, H. S. Poh, A. Ling, and C. Kurtsiefer, Fibre polarisation state compensation in entanglement-based quantum key distribution, Opt. Express **29**, 37075 (2021).

[53] E. Bersin, M. Grein, M. Sutula, R. Murphy, Y. Q. Huan, M. Stevens, A. Suleymanzade, C. Lee, R. Riedinger, D. J. Starling, P.-J. Stas, C. M. Knaut, N. Sinclair, D. R. Assumpcao, Y.-C. Wei, E. N. Knall, B. Machielse, D. D. Sukachev, D. S. Levonian, M. K. Bhaskar, M. Lončar, S. Hamilton, M. Lukin, D. Englund, and P. B. Dixon, Development of a Boston-area 50-km fiber quantum network testbed, Phys. Rev. Appl. **21**, 014024 (2024).

[54] Y.-A. Chen, Q. Zhang, T.-Y. Chen, W.-Q. Cai, S.-K. Liao, J. Zhang, K. Chen, J. Yin, J.-G. Ren, Z. Chen, S.-L. Han, Q. Yu, K. Liang, F. Zhou, X. Yuan, M.-S. Zhao, T.-Y. Wang, X. Jiang, L. Zhang, W.-Y. Liu, Y. Li, Q. Shen, Y. Cao, C.-Y. Lu, R. Shu, J.-Y. Wang, L. Li, N.-L. Liu, F. Xu, W.-B. Wang, C.-Z. Peng, and J.-W. Pan, An integrated space-to-ground quantum communication network over 4,600 kilometres, Nature **589**, 214 (2021).

[55] J. F. Clauser, M. A. Horne, A. Shimony, and R. A. Holt, Proposed experiment to test local hidden-variable theories, Phys. Rev. Lett. **23**, 880 (1969).

[56] C. H. Bennett, G. Brassard, S. Popescu, B. Schumacher, J. A. Smolin, and W. K. Wootters, Purification of noisy entanglement and faithful teleportation via noisy channels, Phys. Rev. Lett. **76**, 722 (1996).

[57] A. Reiserer and G. Rempe, Cavity-based quantum networks with single atoms and optical photons, Rev. Mod. Phys. **87**, 1379 (2015).

[58] M. Saffman, T. G. Walker, and K. Mølmer, Quantum information with Rydberg atoms, Rev. Mod. Phys. **82**, 2313 (2010).

[59] W. Huie, S. G. Menon, H. Bernien, and J. P. Covey, Multiplexed telecommunication-band quantum networking with atom arrays in optical cavities, Phys. Rev. Res. **3**, 043154 (2021).

[60] J. Ramette, J. Sinclair, Z. Vendeiro, A. Rudelis, M. Cetina, and V. Vuletić, Any-to-any connected cavity-mediated architecture for quantum computing with trapped ions or Rydberg arrays, PRX Quantum **3**, 010344 (2022).

[61] D. Burchardt, Ph.D. thesis, Ludwig-Maximilians-Universität München, Germany, 2018.

[62] J. Hofmann, Ph.D. thesis, Ludwig-Maximilians-Universität München, Germany, 2014.

[63] N. Ortegel, Ph.D. thesis, Ludwig-Maximilians-Universität München, Germany, 2016.